Low Reynolds number turbulence in nonlinear Maxwell-model fluids

Chris Goddard[*] and Ortwin Hess[†]

*Advanced Technology Institute and Department of Physics, Faculty of Engineering and Physical Sciences, University of Surrey, Guildford
GU2 7XH, United Kingdom*

Siegfried Hess

Institut für Theoretische Physik, Technische Universität Berlin, Hardenbergstrasse 36, D-10623 Berlin, Germany

A generalized nonlinear Maxwell model which had previously been analyzed for plane Couette geometry is here applied to a lid-driven cavity flow. The full three-dimensional hydrodynamical problem is treated numerically. Depending on the relevant model parameters, both smooth laminar and low Reynolds number turbulent flows are found, strikingly similar to the experimentally observed elastic turbulence phenomena in polymer solutions. Representative results of the calculated flow patterns, as well as measures for the turbulent nature of the flow are presented graphically.

I. INTRODUCTION

It is common knowledge that turbulent flow occurs in simple Newtonian fluids when viscosity does not dominate the dynamics of a material. Inertial turbulence results when inertial forces, caused by high velocities, are greater than viscous forces, and random eddies and flow fluctuations occur. The Reynolds number Re is defined by the ratio of inertial to viscous forces [1]. Typically for pipe flows Re >2300 gives turbulent flow, with an intriguing transition from laminar flow occurring below this [2].

However, other mechanisms can dominate to produce turbulent effects in flows. Elastic forces and nonlinear mechanical instabilities in certain flowing materials (e.g., viscoelastic fluids) have displayed all the properties of developed turbulence, but in contrast, here typically the value of Re only needs to be very small to observe the effect.

Here we present the development and investigation of a spatially resolved model for the rheology of complex fluids, applied to flow geometry which requires the analysis of the full three-dimensional hydrodynamic problem. The equation for the conservation of momentum is supplemented by a constitutive equation for a superposition of stress. The viscoelastic and non-Newtonian behavior, as well as normal stress effects are described by a nonlinear Maxwell model for a contribution to the stress tensor. Another contribution to the stress involves the second Newtonian viscosity which is reached at high frequencies and for high shear rates. The *nonlinear Maxwell model* is a generalized Maxwell model equation which contains temporal and spatial derivatives of the stress tensor and, in particular, terms nonlinear in the stress. By tailoring the details of the nonlinear terms it is possible to describe different fluid properties, with different responses to imposed strains, viz. stationary flow with shear thinning and shear thickening as well as periodic and chaotic stick-slip-like behavior in plane Couette flow. Here the geometry is a lid driven cavity flow, chosen to study shear induced structures. The coupled equations for momentum conservation involving the three components of the velocity field and for the five components of the deviatoric stress tensor, subjected to the appropriate boundary conditions, are solved performing computer calculations based on finite difference approximations and a pressure correction method. Essential spatial terms that were not considered in previous studies of spatially homogeneous flow, as they were not required for plane Couette flow, are now included to complete the studies of inhomogeneous flow. Model parameters are investigated for a range of values to discover two main flow regimes. A laminar-like single vortex develops which gives way to turbulentlike flow when parameters are changed. These flows are visualized using streamlines of velocity fields and intensity plots for stress components. Statistical analysis of the flows is used to give measures for turbulent properties. Such measures lead to the conclusion that the flows are indeed turbulent in nature, having many different size scales and chaotic like dynamics.

The model studied here reveals many features typical for *elastic turbulence* observed in polymer solutions. Recent experiments show flows that can become irregular at low velocity, high viscosity and in a small tank [3,4]. The turbulent flow apparently arose due to the nonlinear mechanical properties of the solution, and developed as polymer molecules were stretched in the primary shear flow, which makes it unstable and causes irregular secondary flow. It is the very back reaction of the polymer molecules on the flow that causes secondary flows [5]. Normal stresses in circular streamlines generate a radial pressure gradient (directed outward or inward), which if large enough can drive more complex flow such as those seen in the Weissenberg effect. The lid driven cavity flow, which is seen to generate a single vortex, is a convenient and well-accepted way of studying this. The study of stretching of polymer molecules by random three-dimensional turbulent flows has shown that the first normal stress difference (N1) is connected to the irregular behavior [6,7]. The stress tensor, including any elastic contributions from polymer molecules drives the elastic turbulence phenomena [8,9], as indicated in the experimental work by Groisman and Steinberg [10–13]. The role of elastic

*c.j.goddard@surrey.ac.uk
†o.hess@surrey.ac.uk

036310-1

forces also explains the drag reduction observed in polymer concentrations [14].

Here we demonstrate that the nonlinear Maxwell model possesses all the rheological properties needed to generate numerical solutions which reveal low Reynolds number turbulence.

II. MODEL EQUATIONS

To model the full hydrodynamical problem, the momentum conservation equation and the incompressibility condition are to used for the flow velocity $\mathbf{v}$,

$$\rho \frac{d\mathbf{v}}{dt} = -\boldsymbol{\nabla} p + \boldsymbol{\nabla} \cdot \boldsymbol{\sigma}, \tag{1}$$

$$\boldsymbol{\nabla} \cdot \mathbf{v} = 0, \tag{2}$$

p is the hydrostatic pressure. The total friction stress $\boldsymbol{\sigma}$ is taken as deviatoric, i.e., as symmetric traceless. A superposition of stress is considered to generalize the Navier-Stokes equation, such that non-Newtonian viscoelastic effects can be included,

$$\boldsymbol{\sigma} = 2\eta_\infty \boldsymbol{\gamma} + \sqrt{2}G_{ref}\boldsymbol{\pi}. \tag{3}$$

Here η_∞ is the second Newtonian viscosity, $\boldsymbol{\gamma}$ is the strain rate tensor, and G_{ref} is a reference value for a shear modulus which need not be specified here. It is introduced for convenience, such that the extra stress $\boldsymbol{\pi}$ is dimensionless. For $\boldsymbol{\pi}$ =0 the Navier-Stokes equation is recovered, with the viscosity η equal to η_∞.

The extra stress $\boldsymbol{\pi}$ is assumed to obey the following generalized Maxwell model,[15,16]

$$\frac{d\boldsymbol{\pi}}{dt} = 2\overline{\boldsymbol{\omega} \times \boldsymbol{\pi}} + 2\kappa\overline{\boldsymbol{\gamma} \cdot \boldsymbol{\pi}} - \tau_0^{-1}(\boldsymbol{\Phi}^\pi - \ell_0^2\nabla^2\boldsymbol{\pi}) + \sqrt{2}\boldsymbol{\gamma} \tag{4}$$

The constitutive relation selected is a choice motivated by previous work on relaxations of the alignment tensor within molecular fluids and nematic liquid crystals where the equations have been derived within the framework of irreversible thermodynamics [17,18] and from a Fokker-Plank equation [19], using the stress-optical law [20,21]. Despite formal and mathematical similarities, the friction stress tensor employed in the liquid crystal problem, e.g., see [22–24], differs from that one used here.

In the above equations, $\boldsymbol{\gamma}$ is the strain rate tensor, $\boldsymbol{\omega}$ is the vorticity, κ is akin to a slip parameter in the Johnson-Segalman model [25], τ_0 is a relaxation time coefficient, ℓ_0 is a characteristic length and $\boldsymbol{\Phi}^\pi \equiv \frac{\partial \Phi}{\partial \pi}$ being the derivative of a potential function with respect to $\boldsymbol{\pi}$, where Φ is the potential function to be chosen. Here the symbol

$$\overline{\cdots}$$

represents the symmetric traceless (deviatoric) part of a tensor, e.g.

$$\overline{x_{ab}} = \frac{1}{2}(x_{ab} + x_{ba}) - \frac{1}{3}x_{cc}\delta_{ab},$$

where δ_{ab} is the unit tensor.

The substantive (advective) derivative is used in Eqs. (1) and (4),

$$\frac{d}{dt}(*) \equiv \frac{\partial(*)}{\partial t} + \mathbf{v} \cdot \boldsymbol{\nabla}(*). \tag{5}$$

The vorticity and the rate of strain are found as follows:

$$\omega = \frac{1}{2}(\nabla \times \mathbf{v}), \qquad \gamma = \overline{\nabla \mathbf{v}}.$$

The "linear" Maxwell model is formed from a potential comprised of the second order scalar invariant I_2,

$$\Phi = \frac{1}{2}AI_2, \tag{6}$$

with a dimensionless coefficient $A > 0$. Thus this implies,

$$\boldsymbol{\Phi}^\pi = \frac{\partial \Phi}{\partial \pi} = A\boldsymbol{\pi}. \tag{7}$$

A nonlinear generalization was invented to treat shear thickening and shear-thinning behavior [15]. A special (simple nontrivial) case for the potential function, which corresponds to an expansion of Φ up to terms of fourth order in $\boldsymbol{\pi}$, using the second and third order invariants I_2 and I_3 reads,

$$\Phi = \frac{1}{2}AI_2 - \frac{1}{3}BI_3 + \frac{1}{4}CI_2^2, \tag{8}$$

which implies,

$$\boldsymbol{\Phi}^\pi = A\boldsymbol{\pi} - \sqrt{6}B\overline{\boldsymbol{\pi} \cdot \boldsymbol{\pi}} + C\boldsymbol{\pi}\,\boldsymbol{\pi} : \boldsymbol{\pi}. \tag{9}$$

In Landau theory the assumption is made that the parameter A depends on the temperature T or the density ρ, according to $A = A_0(1 - T_0/T)$ or $A = A_0(1 - \rho/\rho_0)$ with characteristic temperature T_0 or density ρ_0. The specific dependence of A is not needed but presupposed that it will decrease with decreasing temperature or increasing density. It is also assumed that $A_0 > 0$, $B \neq 0$, and $C > 0$. In Eq. (9) the coefficient A determines whether terms of higher order in $\boldsymbol{\Phi}^\pi$ are of relevance.

Without flow, in a spatially homogeneous system, the stationary solution of the Maxwell-model equation is $\boldsymbol{\Phi}^\pi = 0$. In a fluid state one has $\boldsymbol{\pi} = 0$ and it is a stable solution corresponding to the absolute minimum of the potential function Φ. However, the quantity $\boldsymbol{\Phi}^\pi$ is a nonlinear function of the stress, so solutions with $\boldsymbol{\pi} \neq 0$ are possible. If such a solution is stable, the system possesses a yield stress.

The first investigation of the model (4) with potential (9) was in 1994 [15], when it was introduced to describe shear-thinning and shear-thickening behavior. Applied to the simple case of spatially homogeneous plane Couette flow, it was shown that stress growth, relaxation and hysteresis can be displayed. Also considered were the special cases of vorticity free planar (biaxial) deformational and (uniaxial) elongational flow geometries. Ten years later the model was revisited [16] to consider extra symmetry breaking components of the stress tensor in spatially homogeneous plane Couette flow. Periodic and unstable solutions were explored to reveal chaotic oscillations in the stress, a phenomenon termed Rheochaos.

The same model has recently been used to compare the rheological behavior in fluids with anisotropic and isotropic potentials [26]. This work again was restricted to the plane Couette geometry in spatially homogeneous flow. A bifurcation analysis was performed by Goddard *et al.* [27] (also under spatially homogeneous flow conditions) to explore the range of dynamic solutions present in the model and to show typical bifurcation routes to chaos.

The step to spatially inhomogeneous flows is essential for the study of secondary flows and the shear banding phenomena [28–33], as well as to provide a more physically complete picture of the flow, missing from previous investigations. Spatiotemporal rheochaos has been displayed in similar models for nematogenic fluids [34,35].

To characterize the importance of nonlinearities in the system, scaled variables are introduced. The components of the stress π are expressed in units of the reference value $\pi_c = \frac{2B}{3C}$, for an apparent yield stress which is determined from coefficients B and C in the potential term. The potential term becomes characterized by a single dimensionless parameter, $A^* = A/A_c$, which controls the strength of the linear term in relation to higher order nonlinear terms, as follows:

$$\Phi^\pi = A^* \pi - 3\sqrt{6}\, \overline{\pi \cdot \pi} + 2\pi\, \pi : \pi. \qquad (10)$$

Time is rescaled by $\tau_c = \tau_0 A_c^{-1}$, with $A_c = 2B^2/(9C)$. The shear rate τ_c^{-1}, is denoted by Γ and stress rescaled by G_{ref}, as mentioned above. Length is rescaled by a characteristic length ℓ_{ref}, used as the unit of length for the cavity. During rescaling, the parameter ℓ_0 in Eq. (4) becomes the model parameter ℓ given by $\ell^2 = \ell_0^2 A_c^{-1}$.

In these investigations A^* becomes one of the main parameters studied, to explore the role of nonlinearities in flows. It is recalled that the standard Maxwell model is approached for $A^* \gg 1$. The fascinating dynamic behavior reported in [16] for the plane Couette flow occurs in the range $0 < A^* < 1$. The material is considered to be rheologically homogeneous, that is all the material parameters remain constant throughout the cavity.

The system of equations to be solved consists of the three components of the velocity field and of the five components of the symmetric traceless stress tensor. As in our previous studies [16,27], the latter components, labeled by 0, 1, 2, 3, 4, are chosen such that 1 and 2 are associated with $\pi_{xx} - \pi_{yy}$ and $2\pi_{xy}$, respectively, where the lid is normal to the y direction and it is moving in the x direction. The 0 component is proportional to $2\pi_{zz} - (\pi_{xx} + \pi_{yy})$, the components 3 and 4 are essentially equal to π_{xz} and π_{yz}.

III. TECHNIQUES FOR NUMERICAL SIMULATION

The flow considered is a lid-driven cavity type, which consists of a volume of fluid material confined by impermeable solid walls and a moving top lid as illustrated in Fig. 1. A three-dimensional flow was considered so that all 3 components of the velocity and all five components of the stress tensor become involved, and such that secondary flows will be allowed to develop.

The cavity flow problem is one that has been previously studied quite extensively. Solutions are available using a va-
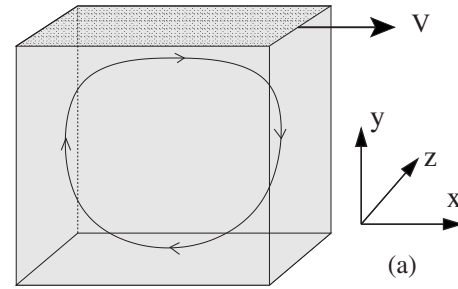

FIG. 1. Illustration of the lid-driven cavity chosen for simulation and an expected resulting laminar flow.

riety of methods which all work around the incompressible Navier-Stokes equations. Most commonly studied is the two dimensional problem.

Taking the example of a 2D cavity in the shape of a square, it is found that in general, for flow of Newtonian-like fluids at low flow rates one observes a single strong vortex centered in the cavity. For a three-dimensional cube cavity the flow would be expected to resemble that of a rotating cylinder, much like the 2D case, but spatially modulated in the extra dimension. For low lid speeds the system tends to reach some steady behavior, resembling laminar flow. For a faster moving lid the flow can become turbulent ([36] used Re=10 000) but this regime is outside of the scope of this investigation, and the focus is on low speed lid movement.

The lid-driven cavity configuration can be achieved experimentally using a conveyor belt arrangement to provide the continuous moving boundary for the top plate. The equations of fluid mechanics are only directly solvable for a limited number of special flows. For more complex flows (and models) the use of computers becomes a requirement [37]. While the partial differential equations still may not be solved analytically, approximate solutions can be found numerically. Systems of algebraic equations, which are solvable on computer, replace the differential equations through discretization methods. The domains of space and time become discrete quantities, where the accuracy of solutions at these points is controlled by the methods used in approximating the original system. In general, a higher accuracy requires more computing resources.

The technique chosen for numerical calculation is the finite difference method. Second-order approximations approximate the spatial derivatives, and a fourth-order Runge-Kutta method is used to approximate the time derivatives.

Other approaches such as the pseudospectral method have recently been used to solve the linear Oldroyd-B model in Kolmogorov flow [38,39] to reveal elastic turbulence. The computational domain is split into cubes of size k, in the unit of length ℓ_{ref}. Each cuboid contains either liquid or solid, with the solid cuboids forming the boundary of the closed cavity. The components of velocity and stress fields are defined at each corner of the cube. In this way, corners of the liquid cube which align with the boundaries of the cavity will correctly match up with the Dirichlet boundary conditions which need to be imposed.

The size of the temporal step h, in reduced units of τ_c, should be small enough to allow fields to diffuse in time

before space, as in the Courant-Friedrichs-Lewy stability condition [40] for solving partial differential equations. For the simulations of this model, tests were made to ensure that choices of k and h are going to be stable by constructing a stability diagram. Many simulations were investigated with different choices of h and k and the stability outcome recorded. A line of stability is found which gives the condition that the time step h should obey $h < 1.5k^2$ in reduced units. The balance can now easily be chosen to ensure sufficient spatial resolution for a given problem, and finding the most efficient time step to ensure stability.

The effect of choosing different values of k and h was compared using slices of the velocity components, where very good agreement was seen. The spatial grid step has therefore been fixed to $k = 0.1$, with a resolution of 50 grid points for each axis, and the temporal step to $h = 0.005$ in the following calculations.

The discretized pressure field has its points staggered such that the pressure is defined at the center of each cube. This allows for the Neumann boundary conditions to be applied correctly on the faces of all solid cuboids. The pressure term is used in a way that continuity is also ensured through a pressure correction method [37]. A resulting Poisson equation can be solved efficiently through a successive over relaxation (SOR) method, which can easily be parallelized [41]. The pressure in-compressibility condition and the calculation of the pressure is one of the more computationally demanding parts of the calculation, so the most effort had to be applied here in order to get results within acceptable time frames.

Boundary conditions at the fluid-surface interface require that material cannot travel into the solid wall (normal velocity is zero) and a no-slip condition is chosen for tangential motion relative to the velocity of the wall,

$$n_i v_i|_{wall} = 0 \quad \text{or} \quad n_i(V_i - v_i)|_{wall} = 0 \qquad (11)$$

$$v_i|_{wall} = V_i, \qquad (12)$$

where n_i is the local unit normal to the surface and V_i is any imposed velocity of the boundary wall. The no-slip condition is a good first approximation for flows. Experimental evidence has shown that in most cases even though one might expect there to be a slipping mechanism, flows modeled with no-slip conditions match accurately [42], through the argument that in molecular terms the intermolecular forces between liquid and solid wall give a bond which results in the no-slip condition. The value for the components of $\boldsymbol{\pi}$ at the boundary is determined locally using zero gradient Neumann conditions.

The field of boundary conditions in continuum theory for entangled systems is still a developing field, and many approaches can be taken to describe the underlying physical effects. Boundary interactions can be imposed using Neumann, Dirichlet, or Cauchy conditions. The boundary conditions affect features of flow at the boundary layer, and certain phenomena can be suppressed in the same way as changing the anchoring between liquid and solid interfaces [30]. The idea to link with molecular dynamics simulations to form a hybrid model seems promising [43–50]. For a discussion of
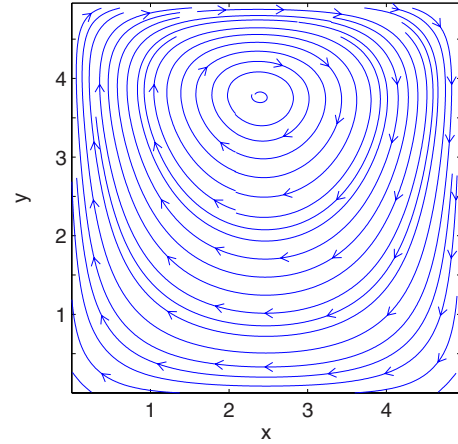

FIG. 2. (Color online) Typical simulation results (streamlines) for large A^* or with the extra stress term removed (by letting $G_{ref} = 0$) showing a laminar flow profile. Here $h = 0.005$, $k = 0.1$, $V_0 = 1.0$ using a cut through the center of the cavity in the x-y plane.

boundary conditions in complex fluids which can lead to an apparent slip see [51].

The velocity of the top plate is set so that $\boldsymbol{\nabla}\mathbf{v}$ vanishes at the sides and corners,

$$v_{lid} = V_0[256x^2(1-x)^2z^2(1-z)^2], \qquad (13)$$

as the discontinuity of the flow field at the upper corners would cause the pressure to diverge. Here x, y, and z have units of the box length, and the center of plate has a v_x velocity component equal to V_0. This provides a slight deviation from traditional lid-driven cavity flows, but the overall effect remains the same.

One method of displaying flows is to take snapshot in time of a 2D slice through the cavity. The most important slice is perpendicular to the moving top plate and parallel with the plate velocity vector. This slice, preferentially taken in the middle of the box, intersects the main flow that occurs in the cavity. The data can then be displayed through intensity plots, which can incorporate contours. Other slices can be used to explore the flow in other directions.

IV. LAMINAR FLOW REGIME

Laminar flows occur when the viscous forces dominate in a material. Any excess energy is dissipated in viscous damping meaning that the flow is characterized by smooth streamlines. Such constant smooth flow has good transport properties, and is important for efficient flows in pipes.

Calculations from this model have shown that laminar flow can occur when parameters are appropriately chosen. As expected, when A^* is large enough ($A^* > 1$) the linear terms in the potential dominate, and the resulting flow becomes laminar. Figure 2 shows typical flow streamlines for simulations with $A^* > 1$ in the x-y plane. Here a single vortex can be seen, off center due to the low value of Re, characteristic of laminar flow profiles. The only stress field present is next to the moving plate, an example is shown later in Fig. 7(c).

To provide a measure of how fast the material in the cavity is flowing, an average velocity v_{av} is calculated by aver-
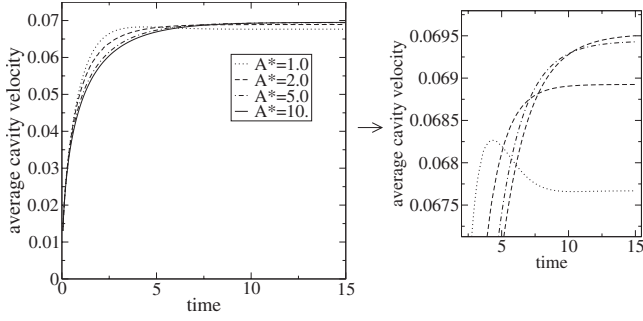
FIG. 3. Average cavity velocity for various values of A^*. Here $\tilde{\kappa}=0.1$, $\ell=0.2$, $V_0=1.0$, $\pi_c=4.0$ and $H_\infty=0.5$. In this and following figures [$\sim$] is used to represent reduced units.
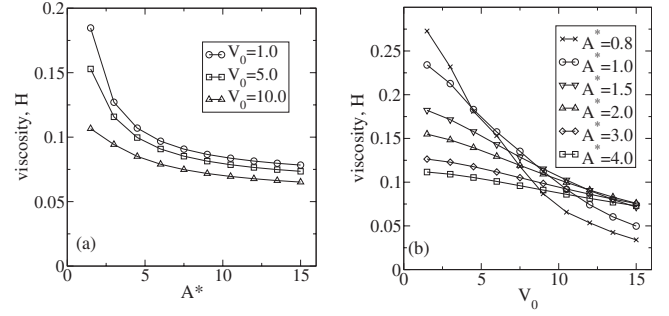

FIG. 4. The average cavity viscosity as a function of (a) A^* and (b) V_0 for various values of driving plate velocity. Here the other parameters are chosen as $\tilde{\kappa}=0.1$, $\ell=0.2$, $\pi_c=4.0$ and $H_\infty=0.5$.

aging the magnitude of the velocity vector at each fluid grid point inside the cavity domain.

Such a measure indicates how well the material is flowing within the cavity. In comparing simulation results this calculation reveals how freely the material is flowing, or how active it is.

From the initial starting conditions of the simulations, which correspond to a system at rest, the imposed forcing of the cavity top-plate increases the fluid velocities in the cavity. Figure 3 shows the average velocity v_{av} as a function of time for a number of different values of A^*.

In the laminar flow regime, the parameter A^* has a small effect on the average cavity velocity. A small velocity overshoot can be seen for the case of $A^*=1.0$, but overall this flow then has a lower average velocity than that of higher values of A^*. The parameter $\tilde{\kappa}$ occurring in the figure caption is related to the parameter κ of Eq. (4) by $\tilde{\kappa}=\kappa/\sqrt{3}$.

Once laminar flow has stabilized (any transient periods have passed), a measurement of the viscosity can be found. The viscosity in the following is presented in units of a reference viscosity $\eta_{ref}=G_{ref}\tau_c$. As such, a dimensionless effective viscosity $H=\eta_{eff}/\eta_{ref}$ is used to express the results.

The viscosity is a material property which, in general, depends on the shear rate. In an experimental setup as considered here, different shear rates occur at different positions within the box. It is desirable to characterize the viscous behavior of a substance within such a device by a single number which is an effective viscosity η_{eff}. The cavity volume average of shear stress in the shearing direction is taken, and divided by a reference shear rate given by the macroscopic value V_0/L_y,

$$\eta_{eff} = \frac{\langle \sqrt{2}\,\pi_c\pi_2 + H_\infty\Gamma_2\rangle}{(V_0/L_y)}, \tag{14}$$

Here L_y is the height of the cavity across the shearing direction, V_0 the plate speed, π_2 and Γ_2 are the components of the extra stress and rate of stress tensors in the shearing direction respectively, their combination in this form gives the xy component of the total stress. If the flow is not laminar then the tensor components of π_2 and Γ_2 will of course be functions of time as well.

The effective viscosity presented next corresponds to the laminar regime. This can be achieved by choosing values

$A^*>1.0$ to ensure that the nonlinear terms are of less importance in the potential function.

The value of the effective viscosity can be plotted as a function of parameter A^*, as displayed in Fig. 4(a). Increasing A^* has the effect of decreasing the effective viscosity, hence thinning the fluid. Different lines correspond to different top-plate speeds, and show that the material has lower viscosities at higher plate speeds.

This dependence on plate speed can be seen as the plate velocity V_0 is changed, and A^* is fixed as in Fig. 4(b). The results show that the material in the cavity behaves as a shear-thinning fluid. The gradient of the line changes as the parameter A^* is adjusted; steeper lines for lower values. For the lowest value of A^* plotted here the line is not so smooth, hinting that there is a more complicated behavior to be found when lowering A^* further.

V. TURBULENT FLOW REGIME

When choosing appropriate model parameters, the calculations reveal that a turbulent-like flow is occurring. A particular example is shown using $A^*=0.2$, $\tilde{\kappa}=0.1$, $\ell=0.2$, $V_0=1.0$, through streamlines and intensity plots in Fig. 5. A snapshot in time of the stress components and velocity
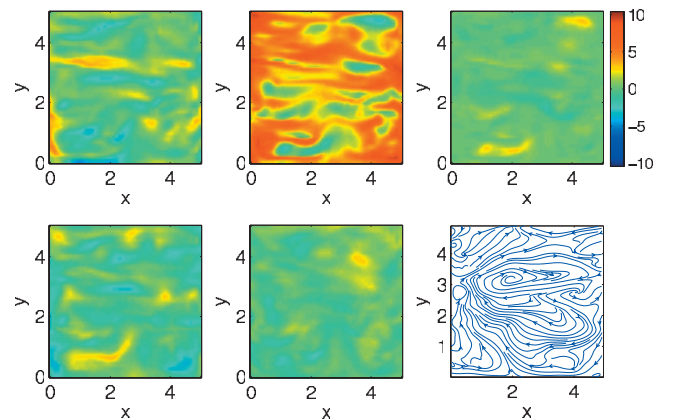

FIG. 5. (Color) Example of stress intensity and velocity streamlines for a low A^* turbulentlike flow. The slice is taken through the center of the cavity in the x-y plane. From top left, σ_{xy}, $N1$, $N2$, σ_{xz}, σ_{yz}, and streamlines.

streamlines are displayed using a slice through the center of the z axis. Slices taken through the other axes display equally turbulentlike behavior. The parameters chosen for this flow correspond to Re ≈ 1.0.

This example has many of the features of turbulence, such as random eddies forming and chaotic flow properties, but occurs at low Re numbers which leads to the hypothesis that the effect is due to the coupling with unstable behavior in the model for the viscoelastic material.

From analytic calculations of the linear response in a spatially homogeneous plane Couette flow with oscillating rates of strain, the apparent relaxation time λ for this model is high when A^* is low. Thus, the Weissenberg number is found to be $Wi = \Gamma / A^*$ for low values of H_∞ [52]. The Weissenberg number is a dimensionless number used in the study of viscoelastic flows. It is given by the ratio of the relaxation time of the fluid to the characteristic rate of deformation. This number gives a characterization for the degree of nonlinearity with respect to the shear rate, and the likely hood of nonlinear rheological behavior and the chance of the elastic turbulence developing. By this measure the nonlinearity is large when A^* is low, and the appearance of turbulence is likely. In plane Couette flow, the nonlinear nature of the equations which are used to phenomenologically model viscoelastic materials lead to instabilities for certain parameter ranges, e.g., $A^* < 1$. This effect has previously been documented for this particular model in a homogeneous flow [16] and explored through bifurcation analysis [27]. The normal stress difference terms became large enough to overcome the dissipative forces of viscosity and create secondary flows from differences in the stress, with instabilities causing the system to show spatial chaos. These then display themselves in the form of vortex structures appearing in the cavity, forming a kind of soft turbulence disordered in space and time.

VI. PARAMETER SCANS

Scanning parameters reveals a host of information in simulations, much like experimenting with real apparatus. We use various statistical measures commonly used for analysis of inertial turbulence. These include measures of velocity fluctuations, distributions and spatial and temporal correlations. For the estimation of size scales present in the cavity, the autocorrelation data are analyzed for its osculation parabola intercept [53] and area under curve yielding smallest and largest eddy approximations, respectively.

In the following we outline the findings from independently changing the three variables A^*, ℓ and V_0.

A. Model parameter—A^*

The parameter A^* controls the shape of the relaxation potential Φ^π for the extra stress π by adjusting the magnitude of the linear part. A number of simulations are run where the only difference is the parameter A^*. The other parameters are fixed at $V_0 = 1.0$, $\ell = 0.2$, and $\tilde{\kappa} = 0.1$.

There is seen to be a clear cutoff point where flow switches between laminar or turbulent/chaotic. In the turbulent case there is an irregular temporal and spatial variation
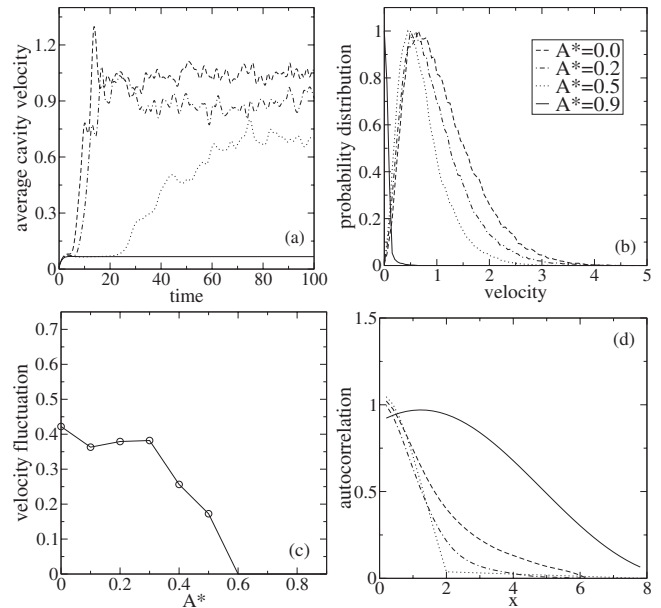

FIG. 6. (a) Average cavity velocity, (b) velocity distribution, (c) velocity fluctuation and (d) autocorrelation results for various values of A^*.

in the stress [e.g., Fig. 5], with the first normal stress difference being the dominant of the stress components, indicating that this is one of the main causes for the resulting secondary flows. In the high A^* laminar flows, the stress plots show no noticeable stress contributions, except near the moving boundary.

Information gained from the velocity field is shown in Fig. 6. Here the average cavity velocity is computed as function of time to show that this quantity fluctuates for the turbulent flow, but not for laminar flow. The overall velocity is also higher in the turbulent flows than the laminar flows. Measuring the velocity distributions reveals a shift in the mean value from close to zero to around 0.6, depending on the value of A^*. Finally measuring the velocity fluctuations as a function of A^* shows how the cutoff occurs at around $A^* = 0.6$, with a general decrease in velocity fluctuation as A^* is reduced to this point.

The spatial chaos in the cavity appears to be present only when there is a time-dependent behavior in the simulations. The material parameter regimes for three-dimensional (3D) chaos are in good agreement with the ranges found for spatially homogeneous plane Couette flow as in [16]. In regions of the cavity, specific local velocity gradients are thought to trigger the nonlinear behavior leading to normal stresses, which then spread through the cavity.

Measurement of the spatial autocorrelation in the flow direction is displayed in Fig. 6(d), where two types of result appear. The longitudinal velocity correlation,

$$f(x) = \overline{v(\xi_1) v(\xi_1 - x)} / \overline{(v')^2} \qquad (15)$$

is calculated using an averaging with respect to time. Here ξ_i is a base coordinate and v' is the fluctuation from mean. The size scale of the smallest eddies, λ_f, can be estimated from

the osculating parabola intercept [53]. The smallest eddies are clearly smaller in size for turbulent flows. The size scale of the largest eddies, Λ_f, can also be estimated by considering the area under the curve. The largest eddies are measured larger in size for laminar flows. These results are very much expected as the laminar flow only has a single steady vortex occupying the whole cavity.

B. Model parameter—ℓ

The stress diffusivity term with coefficient ℓ is added for physical reasons and it is needed for numerical stability. Changing the value of ℓ has a direct effect on the size scales of the features in the cavity and is thus referred to as a characteristic size parameter. As can be seen in Fig. 7, the larger ℓ is, the larger the scale of the features. In the latter figure, a large magnitude of ℓ produces a laminar flow. Other parameters are fixed at $V_0=1.0$, $A^*=0.1$ and $\widetilde{\kappa}=0.1$.

Analysis of the velocity fields shows that the fluctuations increase as ℓ is increased, but then at a cutoff point of around $\ell=0.6$ the solutions suddenly become laminar in flow, which can be seen also in the average cavity velocity plot. There is a small positive shift in the peak of the velocity distribution as ℓ is increased. Here the distinction between laminar flow and turbulent flow is again obvious.

The autocorrelation data in Fig. 8(d) show the difference between laminar and turbulent flows is still present. For $\ell > 0.6$ the flows are laminar in nature, so the autocorrelations are very similar. In the turbulent flow as ℓ is being changed, the size scales are being changed, but its dependence is not so clear.

Too small a value of ℓ should be avoided to reduce the chance of unwanted artifacts appearing in the solutions. The diffusive term is present for stability, and as such it should be ensured that the value of its coefficient ℓ is always greater than that of the spatial grid step k. Too large a value of ℓ and any extra stress generated is quickly diffused away. The choice for ℓ is therefore quite critical.

C. Model parameter—V_0

The parameter V_0 alters the velocity of the moving plate on the top of the cavity, and ultimately the Reynolds number of the flow in the cavity. For low values of V_0 the average velocity in the cavity is also low, and as shown before these equations show chaotic solutions when the strain rate is low. Other parameters are fixed at $A^*=0.1$, $\ell=0.2$, and $\widetilde{\kappa}=0.1$.

Increasing V_0 raises the average velocity in the whole cavity and linear effects begin to dominate the flow. In the bottom of the cavity the flow still remains turbulentlike, and this affects the results of the statistical analysis. In Fig. 10 the average cavity velocity is increased by raising V_0. This does not appear to shift the peak in the probability too much, but instead to excite the higher velocities. This is consistent with a larger vortex forming at the top, while there is still turbulentlike behavior below. The fluctuations on the velocity remain because of this, but finally begin to drop at the high end of the scan.
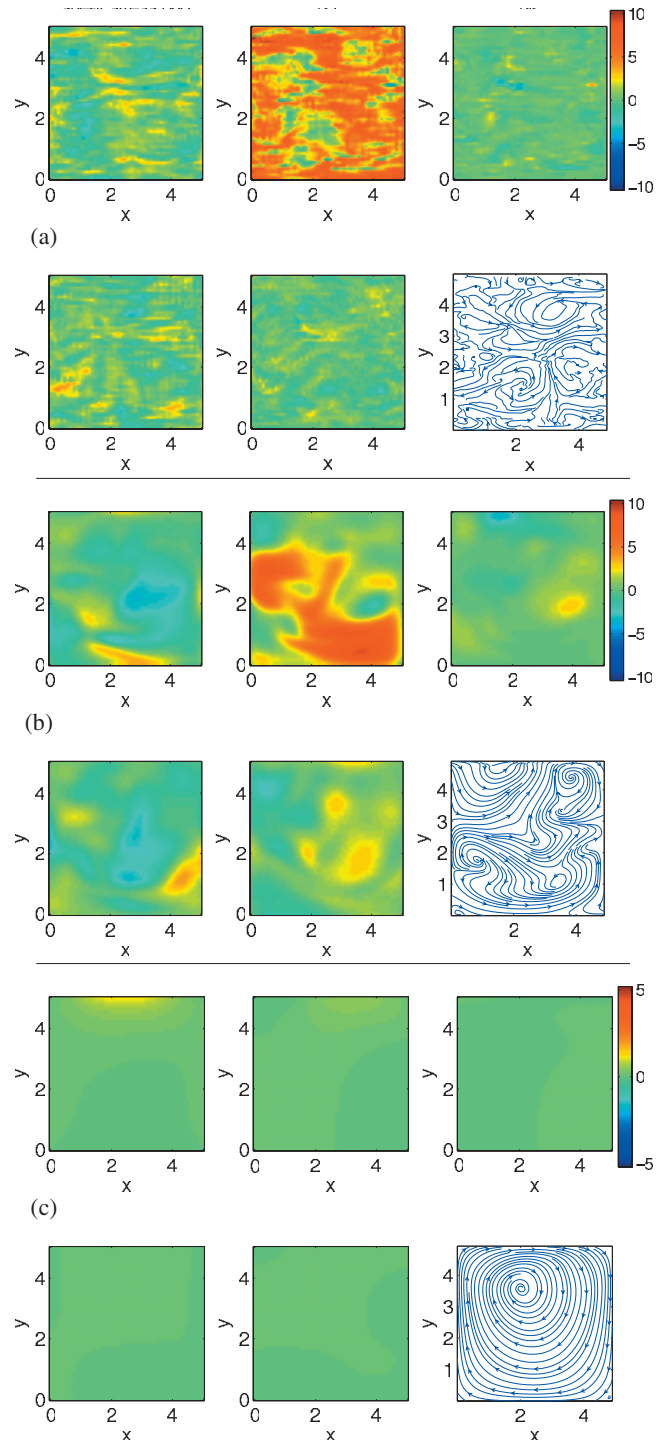

FIG. 7. (Color) Velocity streamlines and the shear stresses and normal stress differences for (a) $\ell=0.1$, (b) $\ell=0.5$ and (c) $\ell=0.6$. For each, from top left, σ_{xy}, N1, N2, σ_{xz}, σ_{yz}, and streamlines.

The autocorrelation plots in Fig. 10(d) show that in general for higher values of V_0 there is an increase in the size of the small and large scale features. This is also confirmed by the streamline and stress plots above.

In summary, the parameter V_0 is changing the value of the average velocity in the cavity by imparting motion on its surface. When the velocity (and hence rate of strain) is high enough the model responds with a steady solution for $\boldsymbol{\pi}$ and
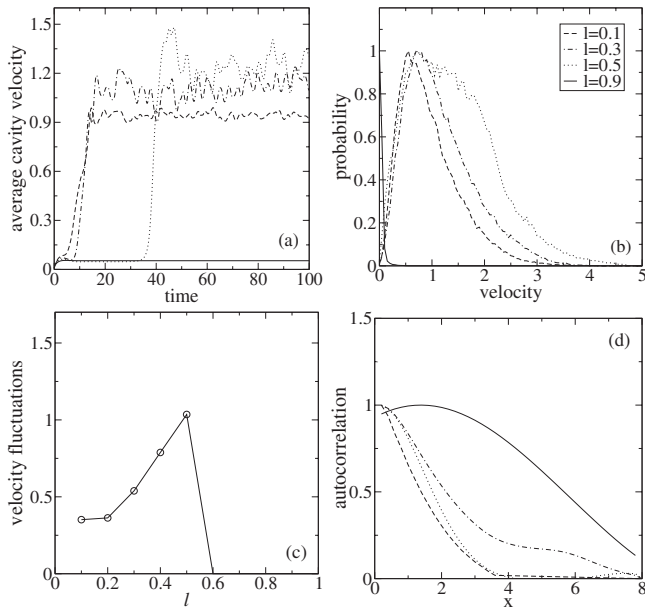
FIG. 8. (a) Average cavity velocity, (b) velocity distribution, (c) velocity fluctuation, and (d) autocorrelation results for various values of ℓ.

therefore the total stress. What is seen in these simulations for higher values of V_0 is that in the top of the cavity the velocity is higher and leads to laminar flow, while lower in the cavity there is less velocity diffusing down and the turbulent regime develops (Fig. 9 and 10). As long as there is a turbulent flow somewhere in the cavity there will be fluctuations in the velocity as seen in the plots, but only the streamline figures can currently tell the full story for its location within the cavity.

VII. SUMMARY AND CONCLUSION

The nonlinear Maxwell model studied here, on the one hand, is rich enough to describe intriguing rheological behavior and low Reynolds number turbulence, on the other hand it is simple enough to be applied in numerical calculations for three-dimensional hydrodynamical problems. The findings seen in our special geometry can be correlated with the rheological properties analyzed in a simple flow. For a
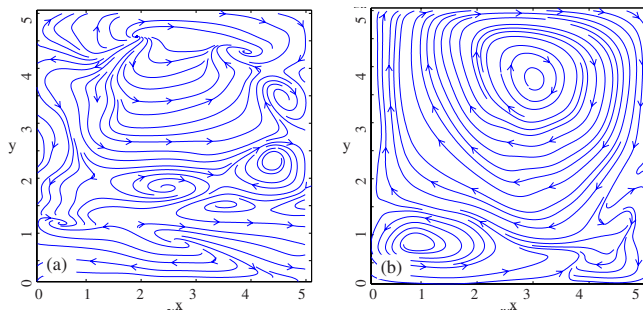

FIG. 9. (Color online) Velocity streamlines and the shear stresses and normal stress differences for (a) $V_0=6.0$ and (b) $V_0=21.0$, cut through the center of the cavity in the x-y plane.
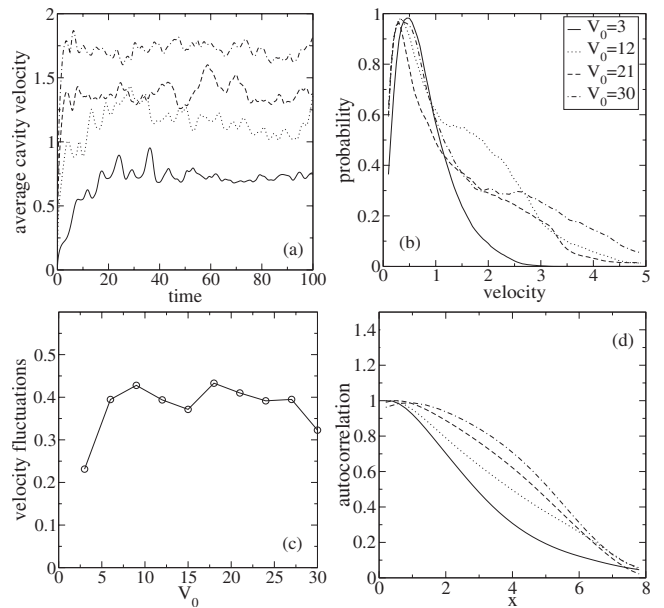

FIG. 10. (a) Average cavity velocity, (b) velocity distribution, (c) velocity fluctuation and (d) autocorrelation results for various values of V_0.

comparison of the dependence of the various types of flow on the parameters $\tilde{\kappa}$, A^*, and π_c, with the occurrence of time-dependent responses in homogeneous plane Couette flow, the stick-slip (tumbling) parameter [26] can be used. From first observations, the parameter A^* correlates well, especially when relating Fig. 6(c) with our results in [27] where the cutoff point is $A^*\approx 0.5$ in each case. The nonlinear chaotic responses that have been shown previously in this model display now themselves in spatially resolved flow in the form of "soft turbulence," producing many vortex structures and eddies.

The importance of a stress diffusion term is displayed, not only for stability, but also to determine the size scale of any features that evolve. The main focus was on the parameter A^* due to its effect on the potential term and the nonlinear terms. This parameter can be seen to "switch" turbulent behavior on when the regime of low values (corresponding to high nonlinearities) was selected.

The onset of turbulence appears to be triggered by regions within the cavity where the local rate of strain corresponds to unstable solutions for $\boldsymbol{\pi}$. More specifically the rate of strain must be low enough to relate to a oscillatory or chaotic response from Eq. (4) as in [27]. When the other parameters are chosen appropriately, this instability in the stress is then large enough in magnitude to overcome the viscous damping forces and results in secondary flows which are irregular in nature and have time-dependent properties. This is confirmed when increasing the lid speed, whereby the local rate of strain (and the Re number) increases globally, and the response of $\boldsymbol{\pi}$ is to be steady state [27]. This result agrees with the many other studies of elastic turbulence and it's occurrence only at low Re [3,54,55].

This work presents a "proof of concept," allowing for future studies of this phenomena to be investigated. It would

be interesting to study how energy is dissipated in the cavity so that an analog could be formed with the work by Kolmogorov [56] for inertial turbulence scaling.

It is also possible to formulate a six component model, by using an additional dynamic equation for the trace of the extra stress tensor. This gives an extra degree of freedom which corresponds to an expansion/contraction of molecules, like in rheological models involving the configurational ten-

sor or a pom-pom model [57–59]. Initial simulations using a six component model reveal that irregular turbulentlike flows are also able to develop.

ACKNOWLEDGMENT

[1] O. Reynolds, Philos. Trans. R. Soc. London **174**, 935 (1883).

[2] T. M. Schneider, B. Eckhardt, and J. A. Yorke, Phys. Rev. Lett. **99**, 034502 (2007).

[3] A. Groisman and V. Steinberg, Nature (London) **405**, 53 (2000).

[4] R. G. Larson, Nature (London) **405**, 27 (2000).

[5] E. Balkovsky, A. Fouxon, and V. Lebedev, Phys. Rev. Lett. **84**, 4765 (2000).

[6] A. Groisman and V. Steinberg, Phys. Rev. Lett. **86**, 934 (2001).

[7] M. Chertkov, Phys. Rev. Lett. **84**, 4761 (2000).

[8] T. Burghelea, E. Segre, and V. Steinberg, Phys. Rev. Lett. **96**, 214502 (2006).

[9] V. S. L'vov, A. Pomyalov, I. Procaccia, and V. Tiberkevich, Phys. Rev. E **71**, 016305 (2005).

[10] A. Groisman and V. Steinberg, New J. Phys. **6**, 29 (2004).

[11] A. Groisman and V. Steinberg, Phys. Fluids **10**, 2451 (1998).

[12] A. Groisman and V. Steinberg, Europhys. Lett. **43**, 165 (1998).

[13] Y. Jun and V. Steinberg, Phys. Rev. Lett. **102**, 124503 (2009).

[14] A. Roy, A. Morozov, W. van Saarloos, and R. G. Larson, Phys. Rev. Lett. **97**, 234501 (2006).

[15] O. Hess and S. Hess, Physica A **207**, 517 (1994).

[16] O. Hess, C. Goddard, and S. Hess, Physica A **366**, 31 (2006).

[17] S. Hess, Z. Naturforsch. **30a**, 728 (1975); **30a**, 1224 (1975).

[18] S. Hess, J. Non-Equilib. Thermodyn. **11**, 175 (1986).

[19] S. Hess, Z. Naturforsch. **31a**, 1034 (1976).

[20] M. Kröger, C. Luap, and R. Muller, Macromolecules **30**, 526 (1997).

[21] G. Ianniruberto and G. Marrucci, J. Non-Newtonian Fluid Mech. **79**, 225 (1998).

[22] C. P. Borgmeyer and S. Hess, J. Non-Equilib. Thermodyn. **20**, 359 (1995).

[23] S. Hess and M. Kröger, J. Phys.: Condens. Matter **16**, S3835 (2004).

[24] S. Heidenreich, P. Ilg, and S. Hess, Phys. Rev. E **73**, 061710 (2006).

[25] M. Johnson and D. Segalman, J. Non-Newtonian Fluid Mech. **2**, 255 (1977).

[26] S. Hess, B. Arlt, S. Heidenreich, P. Ilg, C. Goddard, and O. Hess, Z. Naturforsch. **64a**, 81 (2009).

[27] C. Goddard, O. Hess, A. G. Balanov, and S. Hess, Phys. Rev. E **77**, 026311 (2008).

[28] S. Lerouge, M. Argentina, and J. P. Decruppe, Phys. Rev. Lett. **96**, 088301 (2006).

[29] Y. Hu and A. Lips, J. Rheol. **49**, 1001 (2005).

[30] J. M. Adams, P. D. Olmsted, and S. Fielding, Euromech Colloquium 492—Shear-banding in entangled systems, 2007.

[31] P. D. Olmsted, O. Radulescu, and C.-Y. D. Lu, J. Rheol. **44**, 257 (2000).

[32] L. F. Rossi, G. McKinley, and L. P. Cook, J. Non-Newtonian Fluid Mech. **136**, 79 (2006).

[33] A. Aradian and M. E. Cates, Phys. Rev. E **73**, 041508 (2006).

[34] M. Das, B. Chakrabarti, C. Dasgupta, S. Ramaswamy, and A. K. Sood, Phys. Rev. E **71**, 021707 (2005).

[35] R. Ganapathy, S. Majumdar, and A. K. Sood, Phys. Rev. E **78**, 021504 (2008).

[36] H. Shen and W. Fan, ACTA Aeronaut. Astronaut. Sinica **7**, 140 (1989).

[37] J. H. Ferziger and M. Perić, *Computational Methods for Fluid Dynamics* (Springer, New York, 1997).

[38] S. Berti, A. Bistagnino, G. Boffetta, A. Celani, and S. Musacchio, Phys. Rev. E **77**, 055306(R) (2008).

[39] G. Boffetta, A. Celani, and S. Musacchio, Phys. Rev. Lett. **91**, 034501 (2003).

[40] R. Courant, K. Friedrichs, and H. Lewy, IBM J. Res. Dev. **11**, 215 (1967).

[41] M. Šterk and R. Trobec, Proceedings of the Second International Symposium on Parallel and Distributed Computing, 2003, p. 238 (unpublished).

[42] S. Richardson, J. Fluid Mech. **59**, 707 (1973).

[43] Z. Guo, T. S. Zhao, and Y. Shi, Phys. Rev. E **71**, 035301(R) (2005).

[44] J. C. Slattery, E.-S. Oh, and K. Fu, Chem. Eng. Sci. **59**, 4621 (2004).

[45] T. Werder, J. H. Walther, and P. Koumoutsakos, J. Comput. Phys. **205**, 373 (2005).

[46] R. Delgado-Buscalioni, P. Coveney, and E. Flekkøy, e-print arXiv:cond-mat/0401575.

[47] R. Delgado-Buscalioni and P. V. Coveney, Philos. Trans. R. Soc. London, Ser. A **362**, 1639 (2004).

[48] S. T. O'Connell and P. A. Thompson, Phys. Rev. E **52**, R5792 (1995).

[49] X. Nie, S. Chen, W. E, and M. Robbins, J. Fluid Mech. **500**, 55 (2004).

[50] W. G. Hoover and C. Hoover, Mol. Phys. **101**, 1559 (2003).

[51] S. Heidenreich, P. Ilg, and S. Hess, Phys. Rev. E **75**, 066302 (2007).

[52] C. Goddard, Ph.D. thesis, University of Surrey, 2008.

[53] T. Cebeci, *Analysis of Turbulent Flows* (Elsevier, New York, 2004).

[54] A. Groisman and V. Steinberg, Nature (London) **410**, 905 (2001).

[55] T. Burghelea, E. Segre, I. Bar-Joseph, A. Groisman, and V. Steinberg, Phys. Rev. E **69**, 066305 (2004).

[56] A. Kolmogorov, Dokl. Akad. Nauk SSSR **301**, 299 (1941).

[57] T. C. B. Mcleish and R. G. Larson, J. Rheol. **42**, 81 (1998).

[58] W. Verbeeten, G. Peters, and F. Baaijens, J. Rheol. **45**, 823 (2001).

[59] J. Aguayo, P. Phillips, T. Phillips, B. Snigerev, H. Tamaddon-Jahromi, and M. Webster, J. Comp. Phys. **220**, 586 (2007).